Hindawi
Advances in Civil Engineering
Volume 2022, Article ID 3609682, 19 pages
https://doi.org/10.1155/2022/3609682

Research Article

Temperature Field of Concrete-Filled Steel Tubular Arch Bridges and Its Application

Qian Zhou,[1,2] **Pengcheng Feng**,[1] **Jian-Ting Zhou**,[3] **Shihong Jing**,[4] **Guohui Zheng**,[4] **and Wuzhao Zhou**[4]

[1]*China Communications Second Highway Survey, Design and Research Institute Co., Ltd, Wuhan 430056, China*
[2]*Chongqing Jianzhu College, Chongqing 400072, China*
[3]*State Key Laboratory of Mountain Bridge and Tunnel Engineering, Chongqing Jiaotong University, Chongqing 400074, China*
[4]*Chongqing Yuxiang Double Line Expressway Co., Ltd, Chongqing 400023, China*

Correspondence should be addressed to Jian-Ting Zhou; jtzhou@cqjtu.edu.cn

Received 10 December 2021; Revised 14 May 2022; Accepted 6 June 2022; Published 10 September 2022

Academic Editor: Suvash Chandra Paul

This study aimed to reveal the evolution rule and influence mechanism of temperature field and its effect of long-span concrete-filled steel tubular arch bridges in a plateau area. The temperature field and its effect of large-diameter concrete-filled steel tubular arch bridges under strong radiation, hydration heat, and large temperature difference were studied using the ANSYS transient thermal analysis method. The optimization method on transverse perfusion sequence and perfusion-time interval considering temperature effect was proposed based on stress influence line, equivalent age theory, and energy method. Results showed that the temperature field along the radial direction distributes as a symmetrical three-segment polyline with an influence depth of D/4 under ambient temperature and hydration heat, and it distributes as an asymmetric three-segment polyline with an influence depth of D/8 under solar radiation, ambient temperature, and hydration heat, and this is smaller than the specified value of D/4. The maximum temperature on the sunny side is about 20°C higher than that on the shaded side. The influence of solar radiation absorption coefficient and ambient temperature on the maximum temperature gradient and maximum stress is greater than that of wind speed. The optimization method on transverse perfusion sequence and perfusion-time interval considering temperature effect proposed in this paper is reasonable and convenient for engineering applications.

1. Introduction

Concrete-filled steel tubular (CFST) arch bridges have had broad applications in highway and railway projects in mountainous areas of Western China [1]. Taking the Sichuan-Tibet railway as an example, several long-span CFST arch bridges have been planned for the region. However, the temperature field of CFST arch bridges in plateau and mountain areas is different from the temperature field in other areas due to the former's strong solar radiation and large ambient temperature differences. An arch rib with a large-diameter composed of steel tube and concrete will exhibit unique temperature ranges and trends, so it is important to study the temperature field and its effect of long-span CFST arch bridges in plateau and mountainous area.

It was concluded that environmental parameters had a great influence on the temperature gradient of box girders [2–4]. Full-scale segmental experimental studies of long-term temperature field based on the Yarlung Zangbo River Bridge in Tibet were conducted in August 2018 and January 2019 [5, 6], and the calculation formulas of vertical temperature gradient in summer and winter were proposed. It was pointed out that large temperature differences and cooling temperature differences would lead to large tensile stress and cause voids for these kinds of arch bridges. Full-scale segmental experimental studies of hydration heat temperature field under low temperature based on the Yarlung Zangbo River Bridge in Tibet were carried out [7, 8], and the results indicated that the evolution rule of hydration heat temperature field of large CFST arch bridges was similar

to mass concrete. The computational models of vertical temperature gradient, extreme temperature difference, and transverse temperature gradient of CFST members with different inclination angles and directions were studied, and it was pointed out that the temperature gradient of CFST arch bridges in Chinese standards was underrated [9, 10]. The temperature gradient model of CFST members with large diameter under sunshine was established with finite element analysis [11]. It was pointed out that the temperature gradient increased with an increase of section sizes, during an experimental study on four CFST specimens [12]. It was also noted that the temperature field of circular CFST arch rib under sunshine was nonlinear in time and space and was regular in the radial direction [13]. It was concluded that the distribution of temperature and average temperature of each tube in a four-limb truss arch was close to that of a single circular tube [14]. An improved algorithm of cable force considering temperature effect was proposed based on the deduced theoretical relationship between cable force, arch rib alignment, and temperature change [15, 16]. The influence of steel tube size on temperature field was studied, and it was evinced that the maximum temperature gradient increased with an increase of steel tube diameter [17]. The distribution model of vertical radial temperature gradient of CFST arch bridges in plateau areas with large temperature differences was fitted and relied on data from the Sulongzhu Yellow River Bridge [18].

Much research work on temperature field and its effect of CFST arch bridges have been carried out, and some research results have been obtained. However, most studies used small span arch bridges and did not include multiple factors, and a majority ignored the influence of temperature gradient during concreting and hardening. The temperature field and its effect of large-diameter CFST arch bridges under strong solar radiation, large temperature differences, and hydration heat were studied in this paper. The influence of solar radiation, daily ambient temperature difference, and wind speed on the temperature gradient and its effect during concrete hardening were analyzed. An optimization method on transverse perfusion sequence and perfusion-time interval considering temperature effect was proposed based on the stress influence line of the arch rib, the equivalent age theory of concrete, and the energy method. The research results can provide a theoretical basis for construction of long-span concrete-filled steel tubular arch bridges in mountainous areas.

2. Environmental Parameters

2.1. Solar Radiation. The solar radiation at the summer solstice in Jiacha County, Tibet, with a latitude of 29.15°, a declination angle of the summer solstice of 23.44°, and an altitude of 3200 m was analyzed as an example. The sun shines from 8:00 am to 8:00 pm, the initial temperature is 15°C, and the ground radiation reflection coefficient and solar scattering radiation coefficient are 0.35 and 0.138, respectively. The solar radiation is calculated based on the ASHRAE model [19], and the daily variation of solar radiation intensity on the Earth at the summer solstice is shown in Figure 1. The maximum solar radiation intensity on the Earth appears at 15:00.

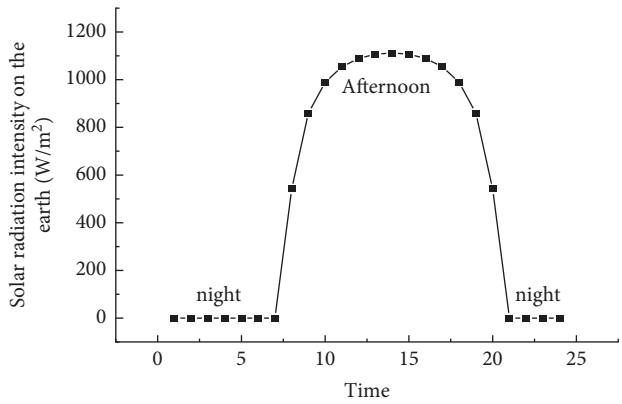

Figure 1: The daily variation of solar radiation.

2.2. Ambient Temperature. From the local historical temperature data and the construction monitoring data of Yarlung Zangbo River Bridge, the common ambient temperature difference and average atmospheric temperature are shown to be 20°C and 22.5°C, respectively. The ambient temperature at each time in a day (see Figure 2) was calculated from the sinusoidal temperature curve [20].

2.3. Hydration Heat. Hydration heat cannot be directly applied in ANSYS [21, 22] but should first be converted to heat generation rate. There are three main steps involved: (i) calculate heat generation rate, (ii) apply heat generation rate, and (iii) create thermal analysis solution.

Heat generation rate can be calculated using the following equation:

$$H_{\mathrm{GEN}} = W\frac{\mathrm{d}Q(t)}{\mathrm{d}t} = WmQ_0e^{-mt}, \tag{1}$$

where HGEN (kJ/(d.m^3)) represents heat generation rate of concrete; m is a constant related to cement type, specific surface, and pouring temperature; Q_0 (kJ/kg) is the complete hydration heat, which is related to the composition of cement materials and can be estimated by a mathematical model [23]; and W (kg/m^3) is cement consumption per unit volume concrete.

Unit conversion as shown in (2) is performed.

$$1\mathrm{W} = 1\frac{\mathrm{J}}{\mathrm{s}} = 10^{-3}\frac{1\,\mathrm{d}}{(24 * 3600)} = 86.4\frac{\mathrm{kJ}}{\mathrm{d}}. \tag{2}$$

Therefore, heat generation rate can be calculated by using the following equation:

$$H_{\mathrm{GEN}} = W\frac{\mathrm{d}Q(t)}{\mathrm{d}t} = \frac{WmQ_0e^{-mt}}{86.4}. \tag{3}$$

HGEN (W/m^3) can be applied on elements by BFE command in ANSYS.

The hydration heat and heat generation rate for the 28 days after concreting are shown in Figures 3 and 4.

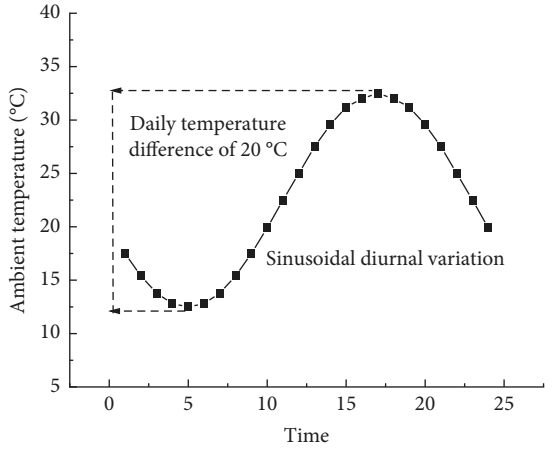

Figure 2: The daily variation of intensity on the Earth ambient temperature.

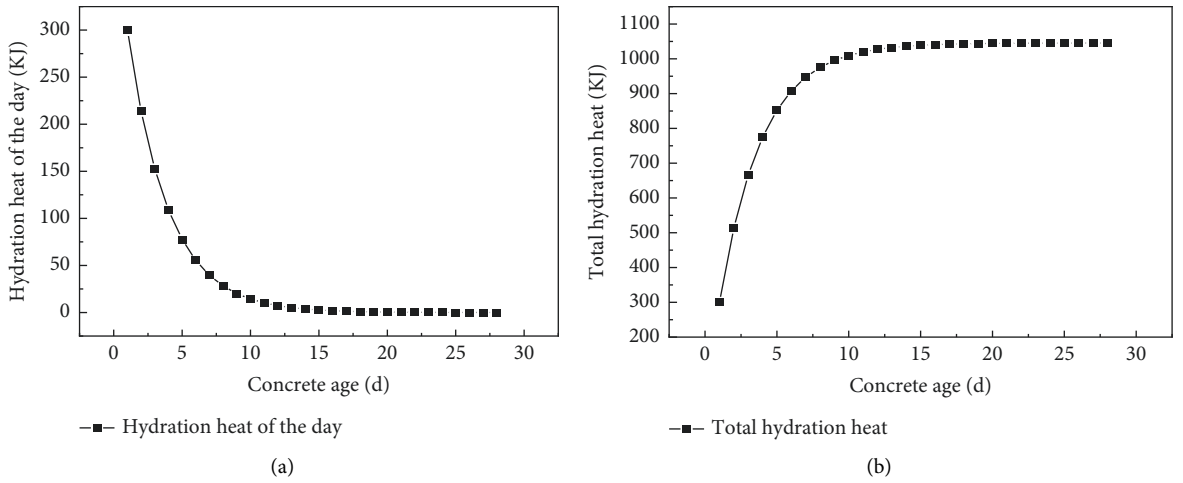

Figure 3: Hydration heat curve: (a) hydration heat released on the day and (b) total hydration heat.

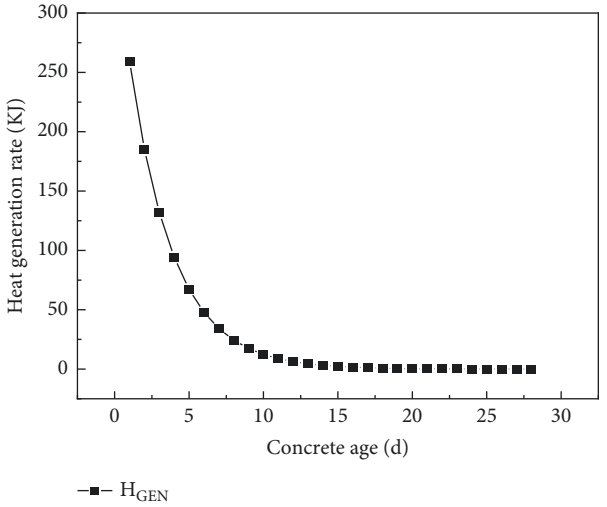

Figure 4: Heat generation rate.

The temperature field of concrete-filled steel tubular arch bridges under the combined action of the above parameters is studied in this paper.

3. Analysis Method

3.1. ANSYS Thermal Analysis Finite Element Method. Considering that the temperature load caused by solar radiation, ambient temperature, and hydration heat changes with time, the transient thermal analysis method [24] was used in this paper. The solar radiation intensity received at different positions of the component is different due to the self-occlusion effect. The conditional statement of IF in parametric language programming is used to identify this self-occlusion effect in this paper. The cosine of solar altitude angle is taken as zero when the calculated value is negative, which indicates that the sun is blocked or the component is on the shaded side.

3.2. The Transient Thermal Analysis Model. The diameter and wall thickness of the member are, respectively, 1.6 m and 28 mm; the radiation absorption coefficient is 0.6; and the wind speed is 3 m/s in the finite element model. The steel tube and concrete are simulated with thermal analysis element SOLID70, and the steel tube and concrete at the interface are connected by VGLUE to realize continuous heat transfer. The network division and number of measuring points of the midspan are shown in Figure 5.

The thermal properties of the steel tube and concrete are shown in Table 1.

3.3. Experimental Verification of the ANSYS Transient Thermal Analysis Method

3.3.1. The Experimental Design. In order to verify the accuracy of the ANSYS transient thermal analysis method proposed in this paper, an experimental study of temperature field was carried out based on a CFST member with a diameter of 50 cm, a length of 1 m, and a wall thickness of 4 mm (see Figure 6). The reinforcement skeleton with 12 temperature sensors (see Figure 7) was put in when pouring to the midspan. Sensor lines with a diameter of 3 mm were led out from the reserved hole and were connected to the main engine of the temperature acquisition system (see Figure 8). The temperature field under strong sunlight was continuously measured for the 6 days after concreting. At the same time, the solar radiation intensity and atmospheric temperature were measured in order to apply thermal boundary conditions in the finite element model.

3.3.2. Comparison between the Test Results and Finite Element Results. The temperature of the concrete in the top interface on the sunny side and temperature of the concrete in the center between the test results and finite element results are shown in Figures 9 and 10, respectively. Results show that the maximum temperature deviation in the top interface on the sunny side and the maximum temperature deviation in the center between the test results and finite element results are about 4°C and 8°C, respectively. The temperature deviation in the center is slightly larger in some nodes as the hydration heat is calculated by an empirical formula. These deviations meet engineering accuracy requirements. The transient thermal analysis algorithm established in this paper can be applied to practical engineering.

4. Temperature Field and Its Effect under Hydration Heat, Strong Radiation, and Large Temperature Difference

4.1. The Distribution of Temperature Field. The cloud diagram of temperature field at 6:00 am and 2 pm three days after concreting is shown in Figure 11.

Analysis shows that the temperature field of the member is evenly distributed in the longitudinal direction, and changes little from 1 am to 8 am. The maximum temperature of the concrete (in the center) is close to 53°C, which is higher than that of the steel tube. The temperature of the steel tube on the sunny side increases gradually from 8 am to 8 pm and reaches the maximum of 53.1°C at 4 pm, but the temperature of the central concrete stays about 53°C from 8 am to 8 pm. The temperature of the steel tube decreases gradually with heat dissipation from 8 pm to 12 pm.

There is a temperature gradient between the top and bottom of the steel tube in Figure 11; this is because the solar radiation intensity at the top of the steel tube is maximal at 2 pm, which at the bottom of the steel tube is 0 (shielding effect).

The temperature of internal concrete is less affected by the external environment and can be considered remaining unchanged. The influence depth (Figure 12) represents the influence range of the external environment on the concrete temperature, and it determines the temperature curve.

The distribution of temperature in the afternoon and at night along each diameter direction is shown in Figures 13 and 14, where the abscissa represents the ratio of the distance from the measuring point to the inner surface of the steel tube on the sunny side to the inner diameter of the steel tube (l/d), and the ordinate represents the temperature of the measuring points.

It can be seen from Figure 13 that the temperature in the afternoon is distributed symmetrically along horizontal radial direction with an influence depth of $D/8$ and decreases first from the interface on the sunny side to its $D/8$, increases to the center, and then decreases from the center to the interface on the shaded side along other radial directions. The maximum temperature of the concrete in the interface on the sunny side is about 55°C; in the center, it is about 50°C; and at the interface on the shaded side, it is close to 35°C. Thus, the maximum temperature on the sunny side is about 20°C higher than that on the shaded side.

It can be seen from Figure 14 that the temperature at noon is distributed symmetrically along each radial direction, and the temperature of the concrete from the center to its $D/4$ remains largely unchanged at above 50°C. The temperature at the interface is low at night, close to 25°C.

To sum up, the radial temperature field under solar radiation, ambient temperature, and hydration heat distributes

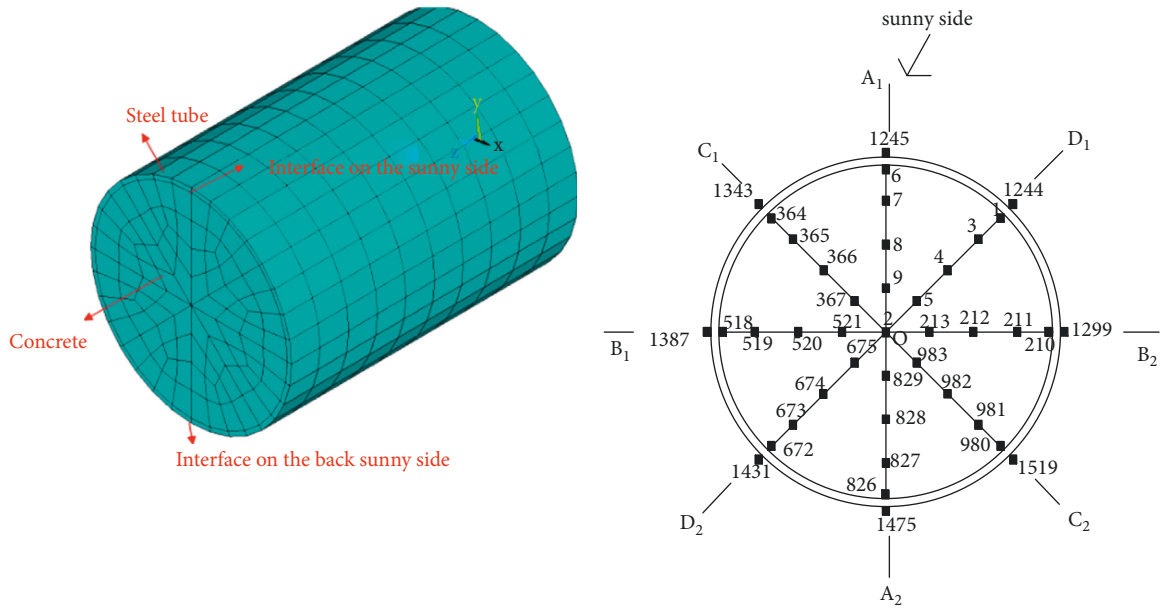

(a) (b)

Figure 5: The network division and number of measuring points of the midspan: (a) network division and (b) number of measuring points of the midspan.

Table 1: The thermal parameters of CFST materials.

Parameters of steel tube	Value	Parameters of concrete	Value
Specific heat capacity	465 J/(kg.K)	Specific heat capacity	1046 J/(kg.K)
Thermal conductivity	80 W/(m.K)	Thermal conductivity	34 W/(m.K)
Density	7850 kN/m^3	Density	2500 kN/m^3
Coefficient of linear expansion	$1.2E-5$	Coefficient of linear expansion	$1E-5$

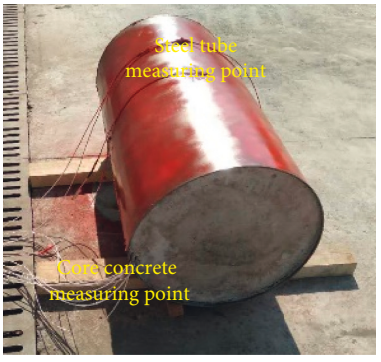

Figure 6: The test component.

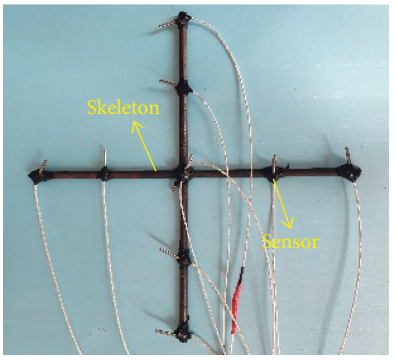

Figure 7: The temperature sensors.

Figure 8: The main engine.

as an asymmetric three-segment polyline with an influence depth of $D/8$, which is less than the specified value of $D/4$, and that under ambient temperature and hydration heat distributes as a symmetrical three-segment polyline with an influence depth of $D/4$.

4.2. Temperature Effect. The indirect coupling method [25] was used for temperature-structure coupling analysis to calculate temperature stress of concrete-filled steel tubular under a temperature gradient. The interface was simulated

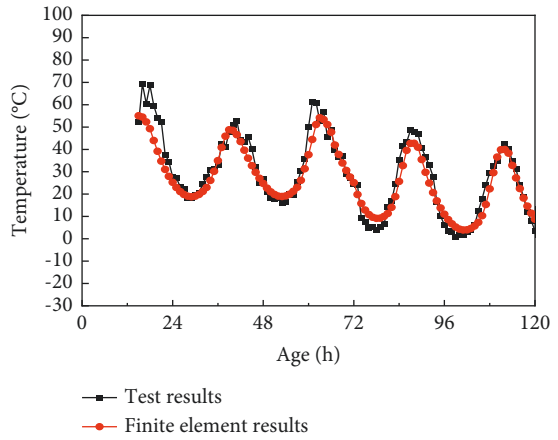

Figure 9: The temperature comparison of the concrete.

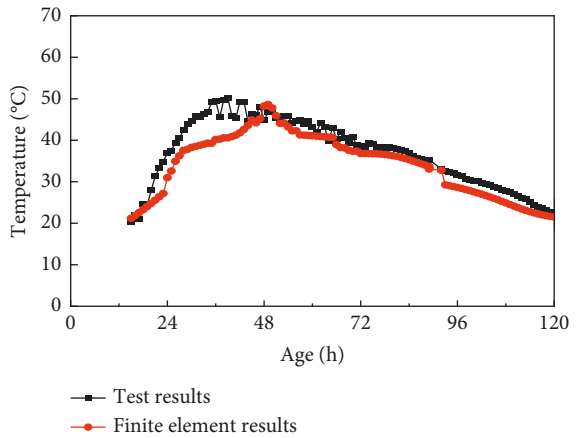

Figure 10: The temperature comparison in the top surface on the sunny side of the concrete in the center.

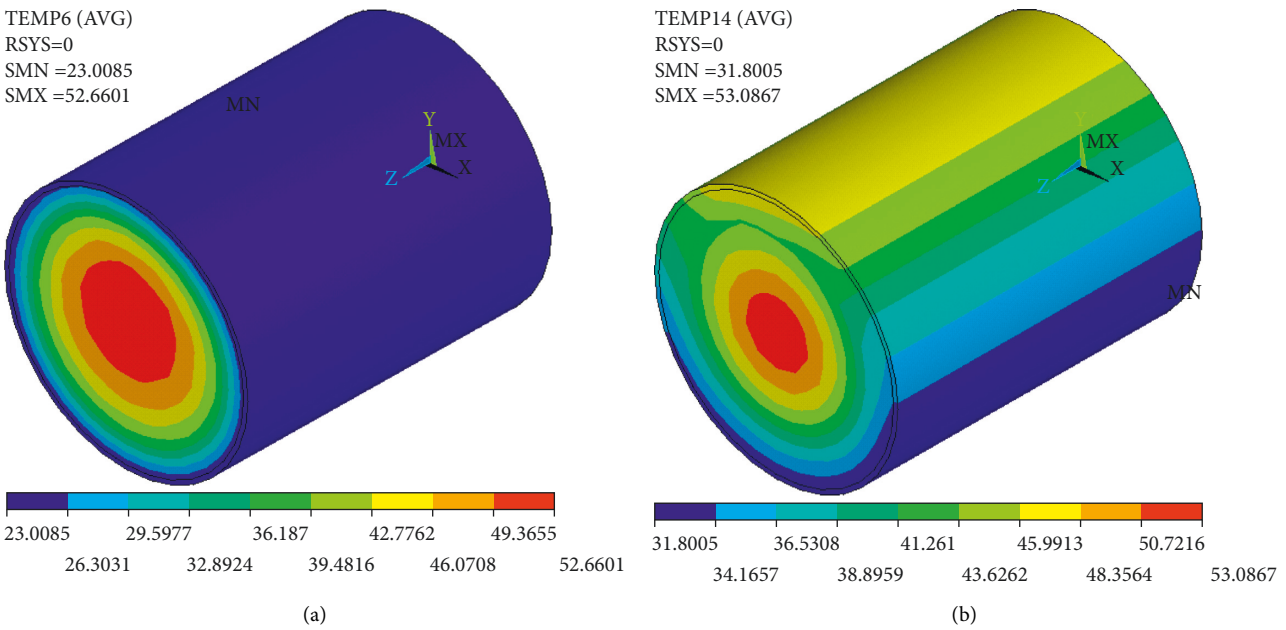

Figure 11: The cloud diagram of temperature field: (a) 6 am and (b) 2 pm.

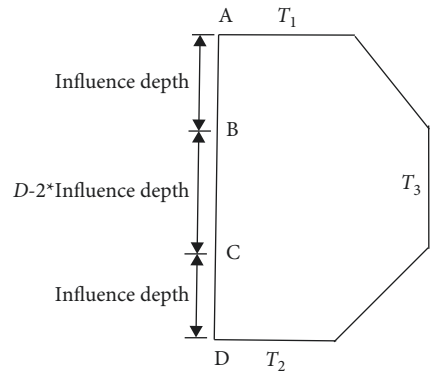

Figure 12: The definition of influence depth.

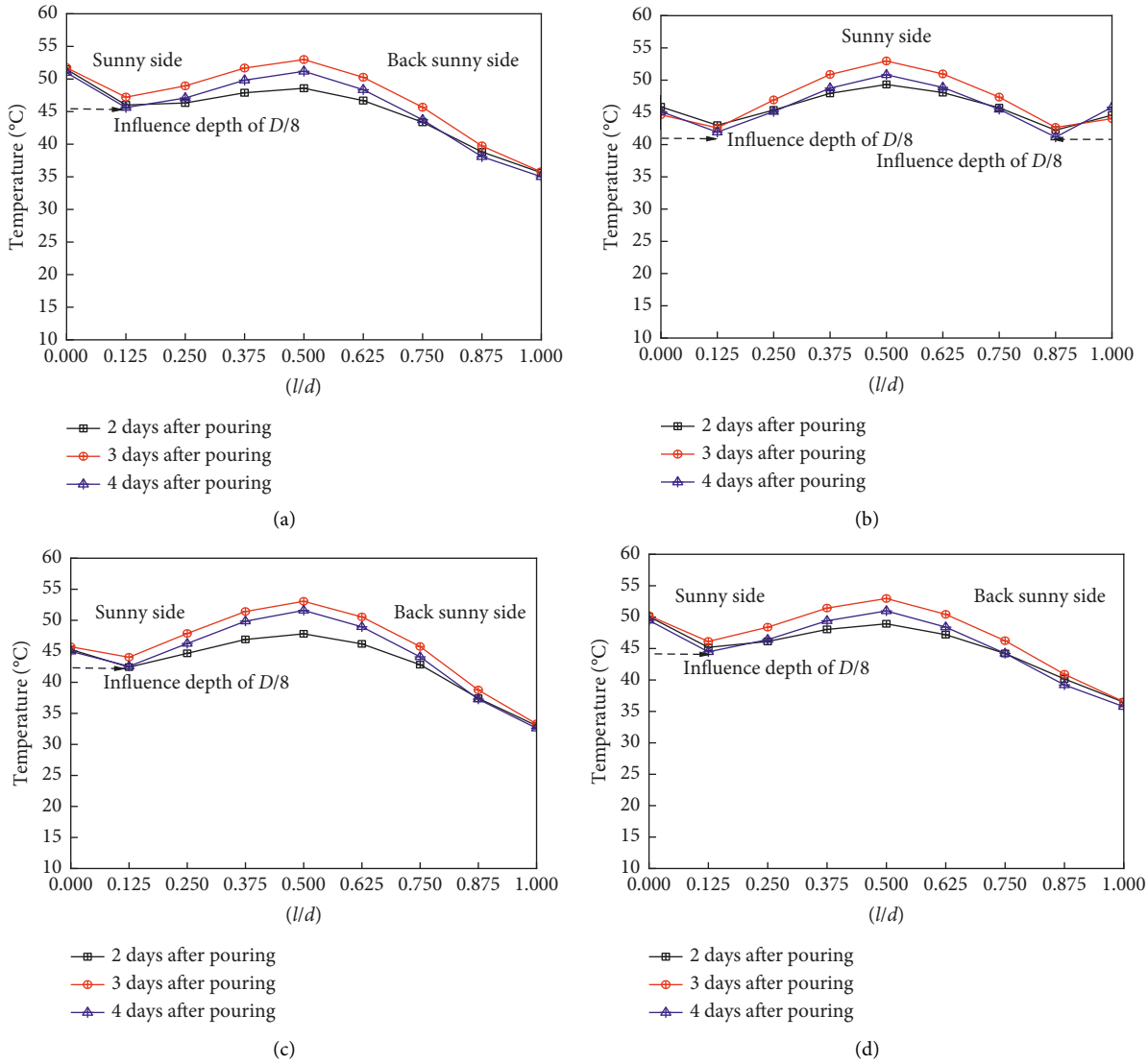

Figure 13: The distribution of the temperature field (2 pm): (a) A1-A2, (b) B1-B2, (c) C1-C2, and (d) D1-D2.

with a surface-surface contact element with an assumed good interfacial bonding. The steel tube being the target surface was simulated with an element of TARGE170, and the core concrete being the contact surface was simulated with an element of CONTA173. The contact pair was simulated by setting the same real constant number for the two different kinds of elements, and the geometric characteristics of the contact element were the same as that of the attached solid

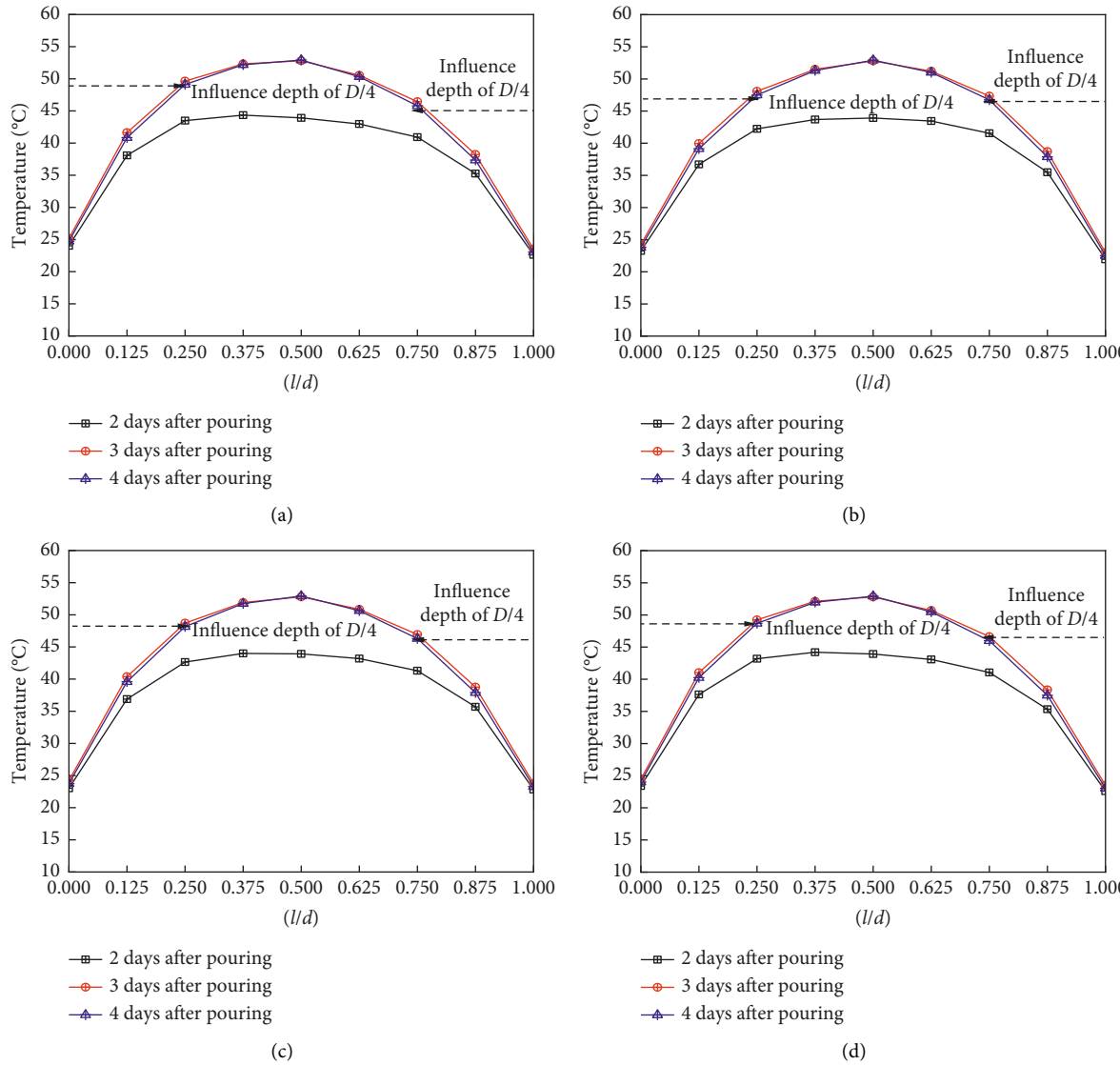

Figure 14: The distribution of temperature field (4 am): (a) A1-A2, (b) B1-B2, (c) C1-C2, and (d) D1-D2.

element [26]. Both steel tube and concrete were transformed into an element of SOLID45 during structural analysis.

Results show that the tensile stress caused by the temperature gradient is large and unevenly distributed in the radial direction, and the maximum tensile stress of concrete is 3.64*E*6 Pa. The stress of the steel tube on the sunny side is greater than that on the shaded side, and the maximum tensile stress is 1.46*E*8 Pa.

4.3. Sensitivity Analysis on Temperature Field and Its Effect

4.3.1. The Design Schemes. According to the investigation, the radiation absorption coefficient of common coatings for a CFST arch bridge is between 0.5 and 0.75. The common daily ambient temperature difference in Tibet is about 20°C in summer and 30°C in winter, but it may exceed 40°C in some occasional extreme environments. The wind speed at the bridge site changes greatly and usually exceeds 3 m/s. The influence of solar radiation absorption coefficient, daily ambient temperature difference, and wind speed on temperature effects pertaining to CFST arch bridges was analyzed using the orthogonal method. The design schemes are shown in Table 2.

Table 2: The design schemes for sensitivity analysis.

Schemes	Solar radiation absorption coefficient	Daily temperature difference of ambient temperature (°C)	Wind speed (m/s)
Scheme 1	0.55	40	3
Scheme 2	0.65	40	3
Scheme 3	0.75	40	3
Scheme 4	0.75	20	3
Scheme 5	0.75	30	3
Scheme 3	0.75	40	3
Scheme 3	0.75	40	3
Scheme 6	0.75	40	5
Scheme 7	0.75	40	7

Table 3: The calculation results of the nonuniform temperature.

Schemes	Temperature of upper steel tube (°C)	Temperature of lower steel tube (°C)	Temperature of left steel tube (°C)	Temperature of right steel tube (°C)	Temperature of upper concrete (°C)	Temperature of lower concrete (°C)	Inner concrete temperature (°C)
4 am							
Scheme 1	11.2	21	11	39.8	11.4	11.4	49.6
Scheme 2	12	22	11	40	11.6	11.6	50.4
Scheme 3	13	25	12	41	12	12	51
Scheme 4	16.2	29	16	41.7	16.4	16.4	49.2
Scheme 5	15.3	26	14	41	14.5	14.5	50
Scheme 6	11.8	20	10	39	11.9	11.9	51
Scheme 7	9	17	8	37	11.9	11.9	50
2 pm							
Scheme 1	48.7	27.8	35	35	46	27.9	48.6
Scheme 2	51.7	28	38	38	49	28.3	50.4
Scheme 3	55	28.4	40	40	52	28.6	55
Scheme 4	46.3	26.1	36	36	45	26.4	48
Scheme 5	51.8	27.6	38	38	51.7	27.8	51
Scheme 6	52	28.4	38	38	51.7	28.6	54.5
Scheme 7	50	28.4	36	36	51	29	54.2

4.3.2. Sensitivity Analysis on Temperature Gradient. The calculation results of the temperature of each scheme in Table 2 under the combined action of hydration heat (at about 72 h concrete age), solar radiation, and ambient temperature are shown in Table 3.

Figure 15 shows the maximum temperature gradient of the different working schemes in Table 2. It can be seen in Figure 15.

(a) The temperature gradient at night is less affected by solar radiation. The maximum temperature gradient in the afternoon increases from 20.7°C to 26.4°C, an increase of 27.5%, and solar radiation absorption increases from 0.55 to 0.75.

(b) The maximum temperature gradient both at night and in the afternoon increase with an increasing daily ambient temperature difference. In the afternoon, the temperature rises from 20.6°C to 26.4°C, an increase of 27.5%, and the daily ambient temperature difference is 20°C to 40°C.

(c) Wind speed mainly affects the heat exchange of outer steel tube and has little effect on temperature gradient of concrete inside.

4.3.3. Sensitivity Analysis on Temperature Effect. The nonuniform temperature under different influence parameters as shown in Table 3 is applied on the finite element model to calculate its temperature effect. The maximum stress on the steel tube and concrete is shown in Figures 16 and 17, respectively. Results show that:

(a) The temperature stress in the afternoon is sensitive to solar radiation, and the stress on the steel tube at 2 pm increases from 172 MPa to 198 MPa, an increase of 15% with solar radiation absorption increasing from 0.55 to 0.75. The stress on the concrete at 2 pm increases from 24.9 MPa to 31.2 MPa, an increase of 25%.

(b) With a daily ambient temperature difference of 20°C to 40°C, the stress on the steel tube at 4 am increases from 128 MPa to 147 MPa, an increase of 14.8%, and the stress on the concrete at 4 am increases from 25 MPa to 32.3 MPa, an increase of 29.2%. The stress on the steel tube at 2 pm increases from 163 MPa to 198 MPa, an increase of 21.4%, and the stress on the concrete at 2 pm increases from 23.7 MPa to 31.2 MPa, an increase of 31.6%.

(c) With wind speed increasing from 3 m/s to 7 m/s, the stress on the steel tube at 4 am decreases from 147 MPa to 127 MPa, a decrease of 15.7%, and the stress of the concrete at 4 am decreases from 32.3 MPa to 27.8 MPa, a decrease of 16.2%. The stress on the steel tube at 2 pm decreases from 198 MPa to 178 MPa, a decrease of 11.2%, and the stress on the concrete at 2 pm decreases from 31.2 MPa to 26.1 MPa, a decrease of 19.5%.

The above research shows that the temperature during concreting and hardening has a great influence on structural stress and deformation. It is necessary to optimize the pouring method of CFST arch bridges in order to reduce the influence of temperature on mechanical properties during concreting and hardening.

The concrete stress during the night is higher than during the day as shown in Fig 17, this is because the temperature of central concrete is higher than that outside due to the hydration heat, and the temperature of outer concrete during the night is lower than it is during the day, so the temperature gradient during the night is greater than the gradient during the day. Consequently, the concrete stress (caused by temperature gradient) during the night is higher than it is during the day.

5. Application Theory of Temperature Field

5.1. Transverse Perfusion Sequence considering Temperature Effect. Influence line reflects the change rule of structural

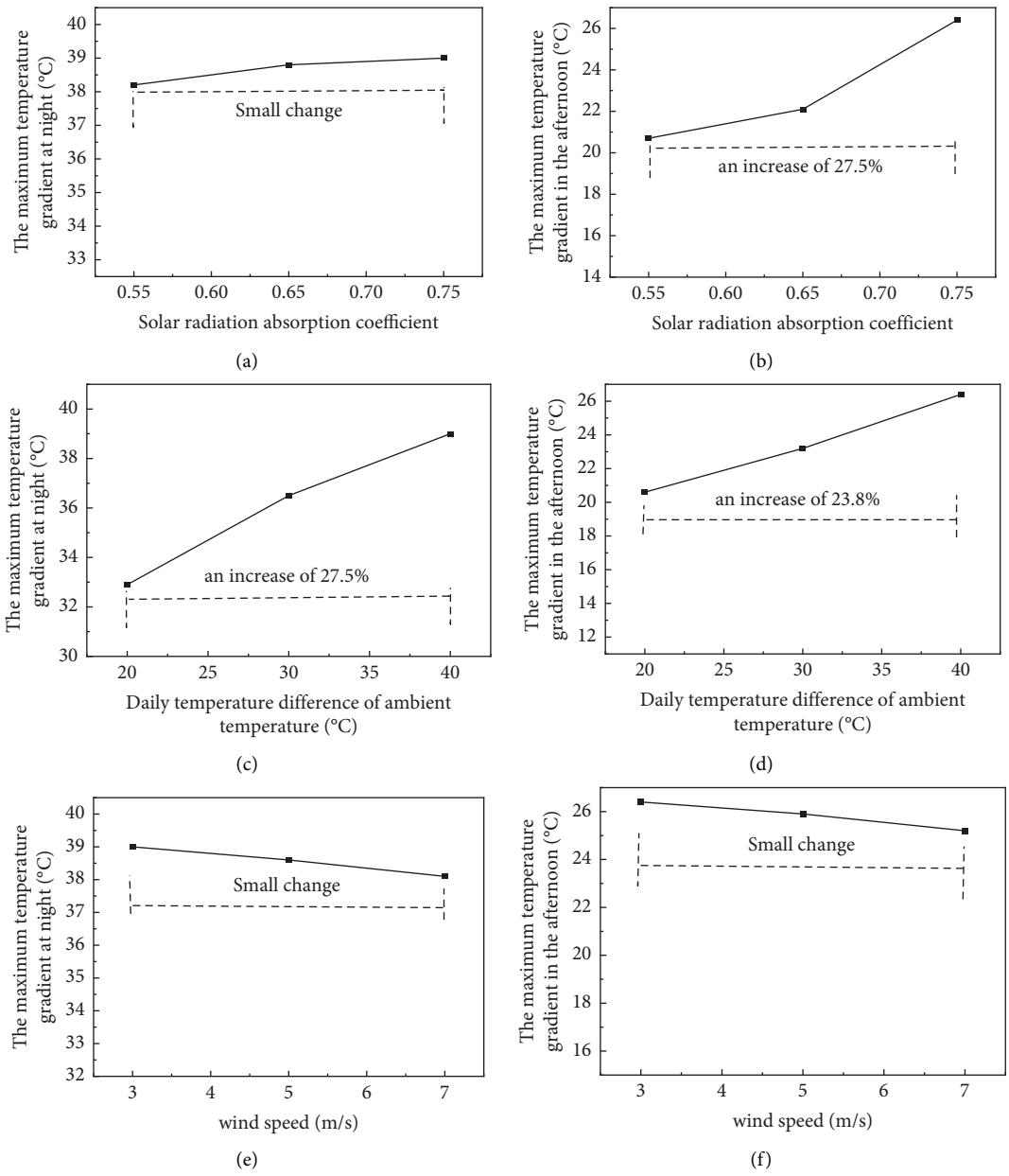

Figure 15: Sensitivity analysis on temperature field: (a) influence of solar radiation absorption coefficient (at night), (b) influence of solar radiation absorption coefficient (in the afternoon), (c) influence of daily temperature difference of ambient temperature (at night), (d) influence of daily temperature difference of ambient temperature (in the afternoon), (e) influence of wind speed (at night), and (f) influence of wind speed (in the afternoon).

deformation and internal force with unit load moving along arch ring. Its abscissa represents the position of focal load, and the ordinate represents influence coefficient [27]. The greater the peak value of the stress influence line, the greater the maximum stress during concreting. To simplify the calculation workload, the peak value of the influence line is proposed as the main index to determine the transverse perfusion sequence.

The analysis detailed in Chapter 4 shows that temperature gradient has a great adverse effect on the mechanical properties of arch ribs. An arch rib with a potentially large temperature gradient should be poured later than an arch rib with a potentially small temperature gradient so that the structure bears unfavorable temperature effects under a larger stiffness; based on this principle, combined with peak value of influence line, the transverse perfusion method considering temperature effect was proposed. For a four-limb truss section (see Figure 18), the pouring order of 1#, 2#, 3#, and 4# arch ribs is to be determined whether the upstream and downstream arch ribs are symmetrically concreted. The calculation flow is shown in Figure 19.

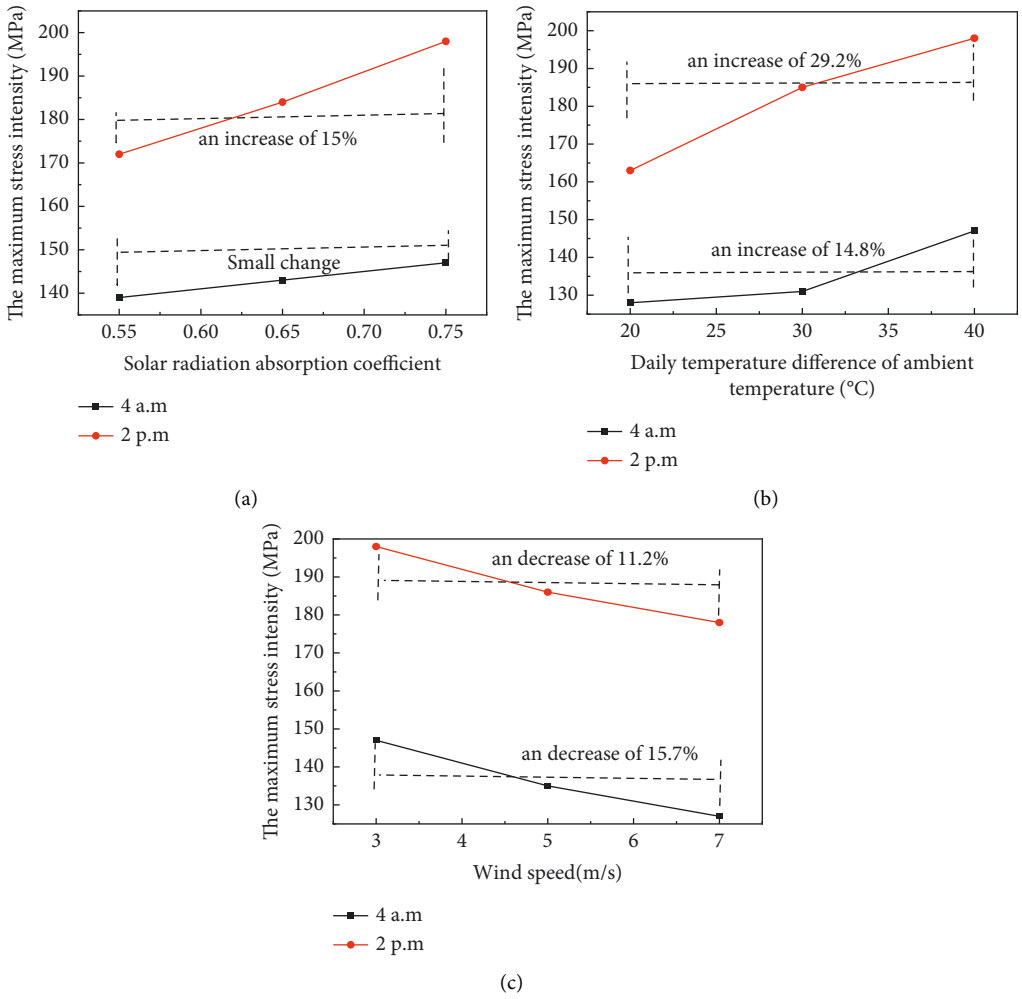

Figure 16: The maximum stress strength intensity of the steel tube: (a) influence of solar radiation absorption coefficient, (b) influence of daily ambient temperature difference, and (c) influence of wind speed.

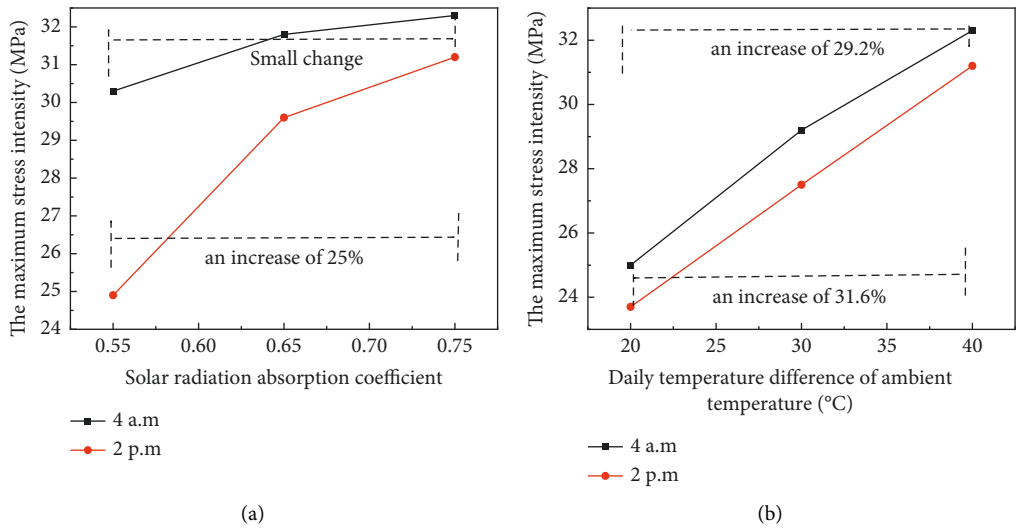

Figure 17: Continued.

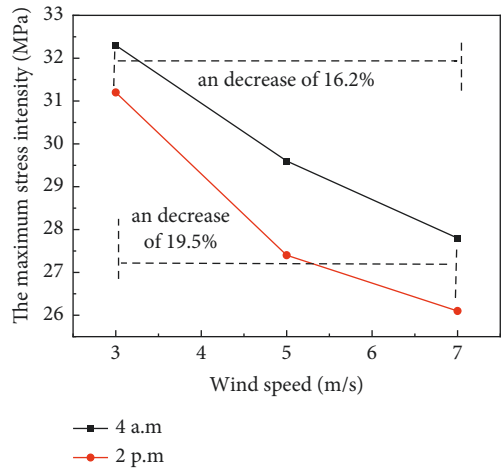

(c)

Figure 17: The maximum stress strength intensity of the concrete: (a) influence of solar radiation absorption coefficient, (b) influence of daily ambient temperature difference, and (c) influence of wind speed.

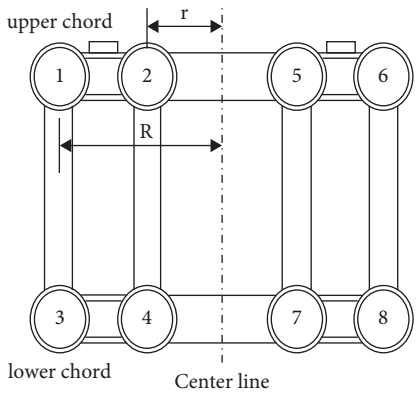

Figure 18: Chord number.

5.2. Study on Perfusion-Time Interval considering Temperature Effect

5.2.1. Relationship between Equivalent Age and Concrete Temperature. Equivalent age is related to concrete maturity. The expression of maturity was shown in equation (4) by Bergstrom [28].

$$M = \sum a_i (T_i + 10), \tag{4}$$

where a_i (day) is curing time, T_i (°C) represents curing temperature, and M (°C.day) represents maturity.

The maturity function of equivalent age was proposed by Freiesleben, and its model was established as shown in equation (5) based on the Arrhenius function [29, 30].

$$t_e = \sum_0^t e^{-E/R\left[1/273+T_e-1/273+T_r\right]} \cdot \Delta t, \tag{5}$$

where E (J/mol) denotes activation energy, which generally takes the value of 33.5 kJ/mol, when T is greater than or equal to 20°C and 33.5 + 1.47 × (20-T) kJ/mol when T is less than 20°C; R is the gas constant 8.314 J/(mol·K); t_e (hour) represents the equivalent age at reference temperature; T_r (°C) is reference temperature of 20°C; T_e (°C) is the real temperature at t; and Δt (°C) represents perfusion-time interval.

5.2.2. Relationship between Early Stiffness and Temperature of Concrete. The relationship between early elastic modulus and age of ordinary concrete was fitted as shown in equation (6) through experimental research [31].

$$E_{c,t} = E_{28}\left(1 - 0.33e^{-0.042t^2}\right). \tag{6}$$

Equation (6) is applicable to C50 concrete under standard curing conditions. However, it is difficult to ensure that concreting and hardening are always under standard curing conditions; thus, the age needs to be converted to equivalent age. After substituting equation (5) into (6), the relationship between early elastic modulus of concrete and temperature and age becomes the following equation:

$$\begin{aligned} E_{c,t} &= E_{28}\left(1 - 0.33e^{-0.042t_e^2}\right) \\ &= E_{28}\left(1 - 0.33e^{-0.042\left(\sum_0^t e^{-E/R\left[1/273+T_e-1/273+T_r\right]}\cdot t\right)^2}\right), \end{aligned} \tag{7}$$

where $E_{c,t}$ and E_{28} are the elastic modulus at time t and 28 days after concreting, respectively; t and t_e are concrete age and equivalent age of concrete, respectively; T_e is the real temperature at t; and T_r is reference temperature, generally 20°C.

5.2.3. Relationship between Element-Weighted Bending Moment Energy and Perfusion-Time Interval and Temperature. The theoretical relationship between element-weighted moment strain energy and elastic modulus is shown in the following equation [32].

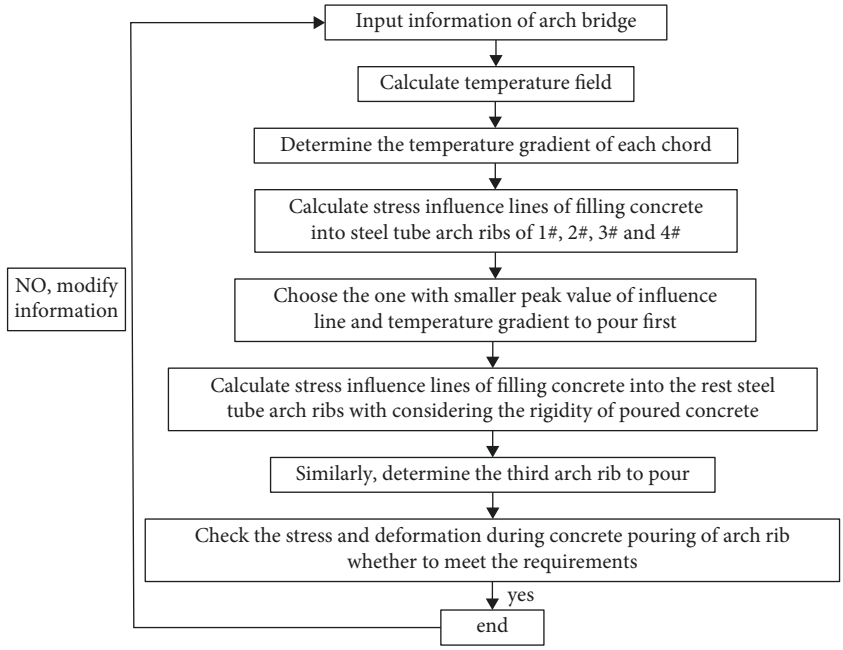

Figure 19: The calculation flowchart of transverse perfusion sequence.

$$U(D_i) = \sum_{i=1}^{m} \frac{k_i l_i}{6E_i I_i}\left(H^2 + HZ + Z^2\right),$$

$$\left.\begin{aligned} 4\frac{EI}{l_i}\varphi_{ii} + 2\frac{EI}{l_i}\varphi_{ij} - \frac{6EI}{l_i^2}[K]^{-1}\{f\} = H \\ 4\frac{EI}{l_i}\varphi_{ij} + 2\frac{EI}{l_i}\varphi_{ii} - \frac{6EI}{l_i^2}[K]^{-1}\{f\} = Z \end{aligned}\right\}, \tag{8}$$

where E is elastic modulus without considering temperature effect; $\{f\}$, I, and $[K]$ represent node load vector, moment of inertia, and overall stiffness matrix, respectively; k_i is the unit weighting coefficient and can be calculated as $k_i = U_i/1/m\sum_1^m U_i$ for m units; l_i is unit length; and φ is the angle between local coordinate system and global coordinate system.

The relationship between concrete age and perfusion-time interval of each arch rib is shown in the following equation:

$$\left.\begin{aligned} t_1 &= D_1 + T_2 + D_2 + T_3 + D_3 + T_4 \\ t_2 &= t_1 - T_1 - D_1 \\ t_3 &= t_1 - T_1 - D_1 - T_2 - D_2 \\ t_4 &= 0 \end{aligned}\right\}, \tag{9}$$

where D_i is the perfusion-time interval from the end of the i-th arch rib to the beginning of the $i+1$-th arch rib; t_i and T_i are concrete age and pouring time of the i-th cast-in-place arch rib, respectively; and t_1 represents the time when perfusion is completed.

After substituting (9) into (7), elastic modulus can be expressed as a function of temperature and perfusion-time interval, as shown in the following equation:

$$E = f(T, D). \tag{10}$$

By substituting (10) into (8), the theoretical relationship between weighted bending moment energy and pouring time and temperature can be obtained. The subsequent equation is as follows:

$$U(D_i) = \sum_{i=1}^{m} \frac{k_i l_i}{6f(T_i, D_i)I_i}\left(H^2 + HZ + Z^2\right),$$

$$\left.\begin{aligned} 4\frac{f(T,D)I}{l_i}\varphi_{ii} + 2\frac{f(T,D)I}{l_i}\varphi_{ij} - \frac{6f(T,D)I}{l_i^2}[K]^{-1}\{f\} = H \\ 4\frac{f(T,D)I}{l_i}\varphi_{ij} + 2\frac{f(T,D)I}{l_i}\varphi_{ii} - \frac{6f(T,D)I}{l_i^2}[K]^{-1}\{f\} = Z \end{aligned}\right\}. \tag{11}$$

In equation (11), there is only one independent variable of the perfusion-time interval once the temperature is determined.

5.2.4. Optimization. The weighted bending moment strain energy of bridges in the finished state (without considering sectional installation) is shown in the following equation: [32].

$$U_0 = \frac{S}{6EI}\sum_{i=1}^{m} k_i\left(M_{ii}^2 + M_{ii}M_{ij} + M_{ij}^2\right), \tag{12}$$

where E, I, and S are concrete design elastic modulus, moment of inertia, and arc length of arch rib, respectively; and M_{ii} and M_{ij} are the bending moments at both ends of rod element.

The perfusion-time interval can be optimized by minimizing the difference of weighted bending moment strain energy between considering section installation and not considering section installation.

$$\left.\begin{aligned} &\min U = \min\left|U\left(D_i\right) - U\left(0\right)\right| \\ &\text{s.t.} D_i \geq 0 \ (i = 1, 2, 3) \end{aligned}\right\}, \tag{13}$$

where $U(D)$ and $U(0)$ represent the weighted bending moment strain energy considering and not considering sectional installation, respectively, and D_i represents the perfusion-time interval.

In conclusion, the optimization algorithm of perfusion-time interval based on temperature field, equivalent age theory, and energy method is shown in Figure 20.

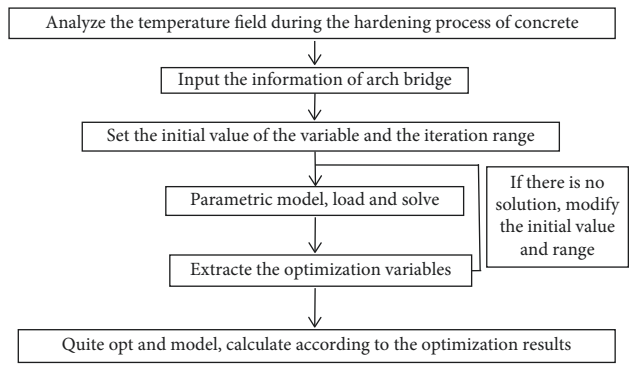

Figure 20: The optimization algorithm of perfusion-time interval.

5.3. Engineering Application

5.3.1. Project Overview and Finite Element Modeling. The main bridge is a half-through catenary concrete-filled steel tubular arch bridge with a clear span of 240 m, a rise span ratio of 1/5, and a design arch axis coefficient of 1.5. The top and bottom chords are 1.016 m in diameter and have a 14 mm wall thickness; the vertical web is 0.508 m in diameter and has a 10 mm wall thickness. The chords are connected with batten plates that have a thickness of 12 mm in transverse, and the two arch ribs are connected with K-shaped empty steel tubes. Q345B steel and C50 microexpansive concrete were used for the main arch rib. The cross section of the arch rib is shown in Figure 18. The actual perfusion sequence was as 1# - 6 # - 2 # - 5 # - 3 # - 8 # - 4 # - 7#, and the upstream and downstream arch ribs were concreted one by one in 2010. It was pointed out that the structural stability during concreting was low, and the perfusion sequence should be better optimized [32].

The steel tube and concrete are simulated with two-dimensional thermal analysis element PLANE55 in the thermal analysis model as shown in Figure 21. In order to facilitate the application of solar radiation load, the surface element SURF151 with isolated nodes was established on the outer and inner surfaces of the component. The steel tube and concrete at the interface are connected by VGLUE to realize continuous heat transfer. The 3D finite element model of the full bridge and main arch ring is shown in Figure 22. The upper and lower chords and the concrete inside are simulated with element beam 44, and the batten plates are simulated with element shell 63.

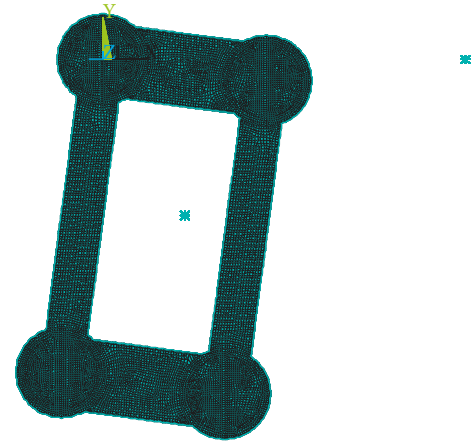

Figure 21: The thermal analysis model.

5.3.2. Temperature Field Analysis. The temperature field at 2:00 am and 2 pm under solar radiation, ambient temperature, and hydration heat of this bridge is shown in Figure 23.

The results show that the daily variations of the temperature field of each chord agree well with each other, and the temperature and its nonuniformity of the upper chords are greater than those of the lower chords for each time. This is because the heat transfer distance is slight with a small diameter, and the temperature of inner concrete is affected by both hydration heat and external environment at the same time. The maximum temperatures of 1#, 2#, 3#, and 4# chords at 2 am are 45.4°C, 44.7°C, 40.8°C, and 41.4°C, respectively, and at 2 pm are 57.6°C, 57.6°C, 44.4°C, and 51.1°C, respectively.

The daily variation of the maximum temperature difference of each chord is shown in Figure 24.

The results show that the daily variation of temperature difference of each chord is basically the same, but there are small differences in value and time of the maximum temperature difference. The maximum temperature gradients of 1# chord and 2# chord on the sunny side are 23.7°C and 21.2°C, respectively, which occurs at 2 pm, and those of 3# chord and 4# chord are 11.8°C and 17.2°C, respectively. This is because the lower chords absorb less radiant heat than the upper chords due to the shielding effect.

5.3.3. Temperature Effect Analysis. The nonuniform temperature field load was applied according to the calculation results given in Chapter 4.3.2, and the maximum temperature gradient of a single chord is 23.7°C. Overall temperature rise of 23.7°C is for comparison, and the maximum stress (SMAX) of the concrete and steel tube is shown in Figure 25.

The comparisons of the deformation and stress between overall temperature rise condition and temperature gradient condition are shown in Figure 26.

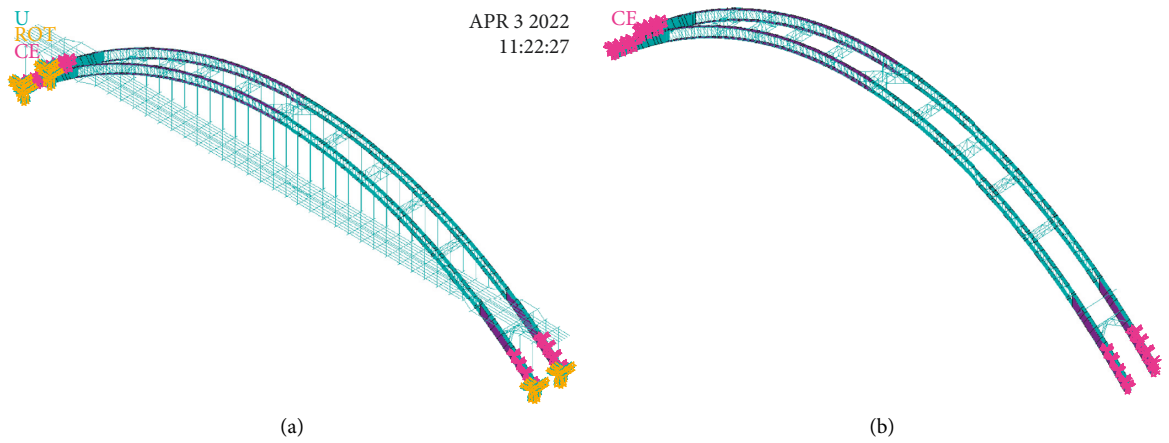

(a) (b)

Figure 22: The 3D finite element model of the full bridge: (a) The full bridge and (b) the main arch ring.

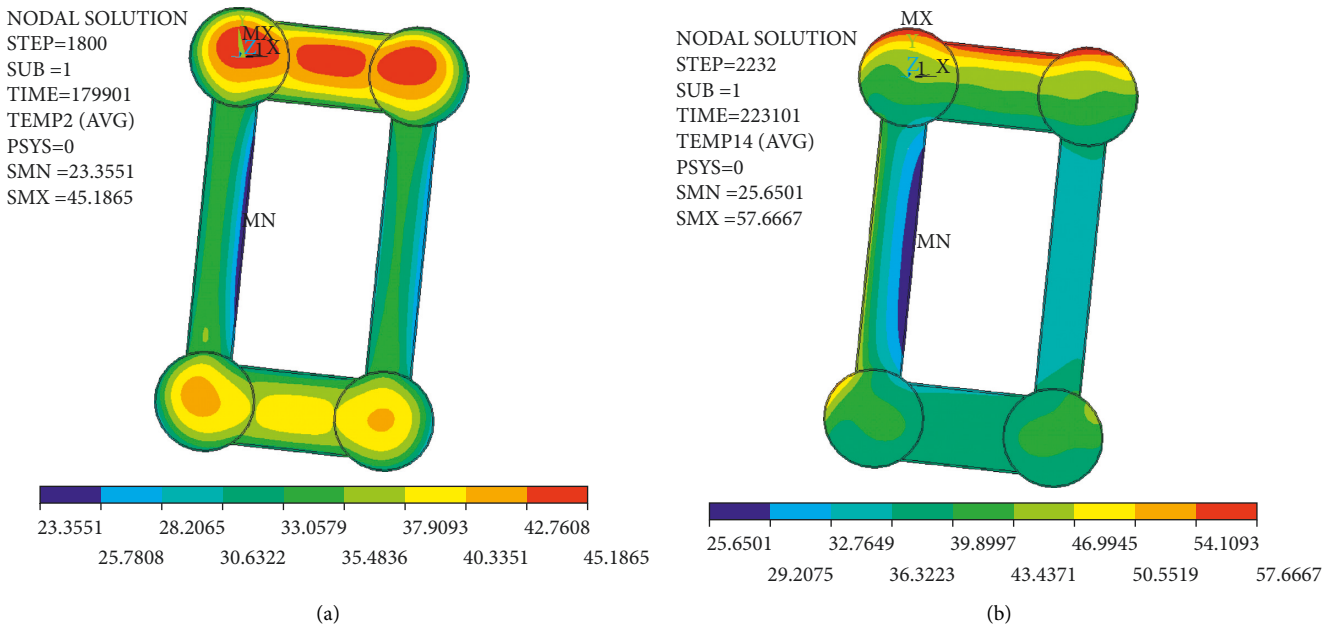

(a) (b)

Figure 23: The temperature field nephogram of four-limb truss section: (a) 2 am and (b) 2 pm.

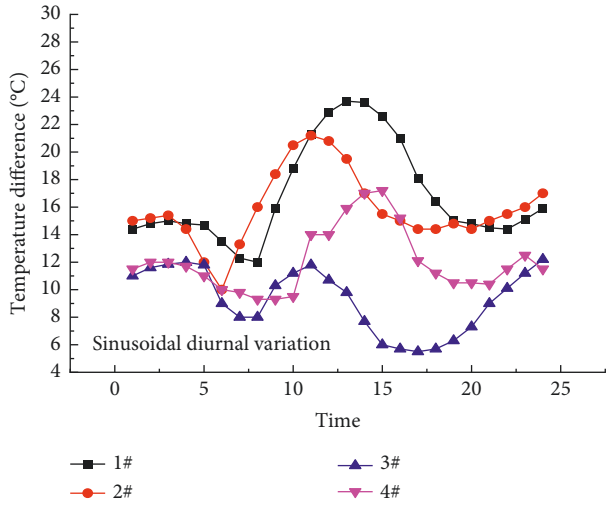

Figure 24: The daily variation of the maximum temperature difference.

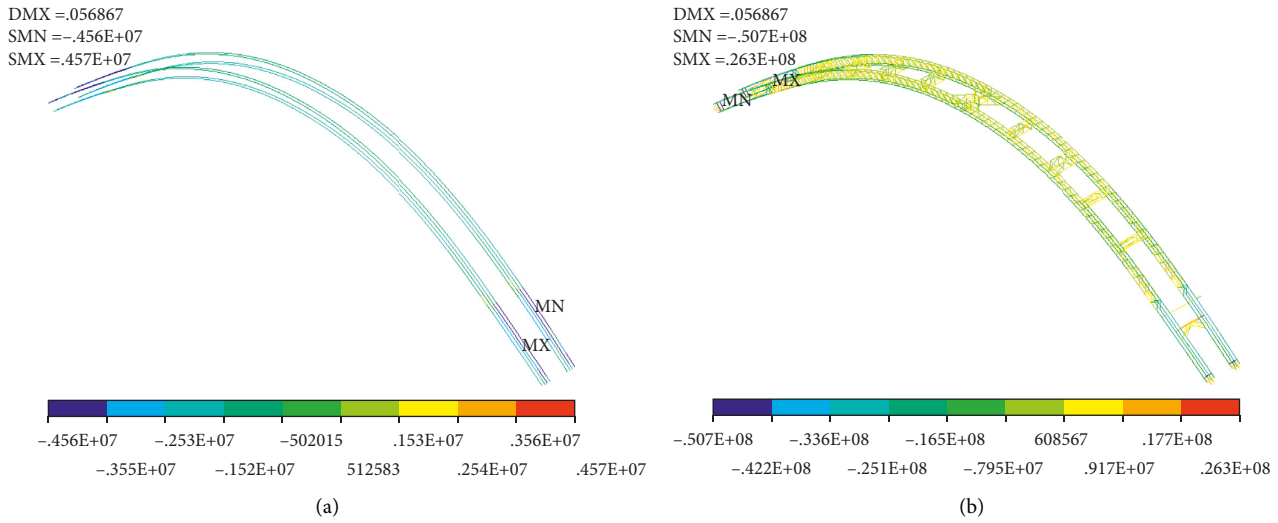

Figure 25: The maximum stress (SMAX) of overall temperature rise of 23.7°C: (a) concrete and (b) steel tube.

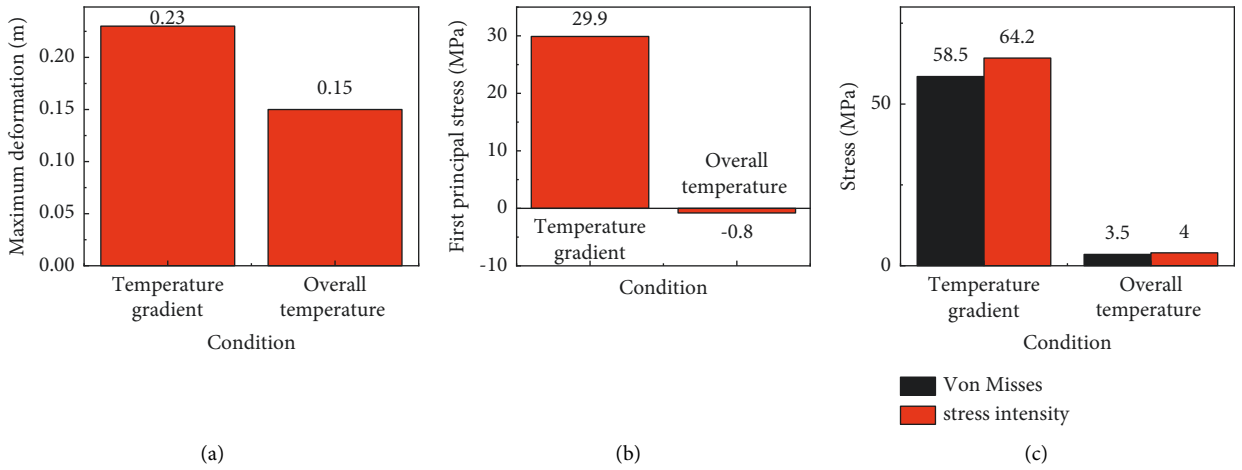

Figure 26: The comparison of calculation results between overall temperature rise of 23.7°C and temperature gradient of 23.7°C (single chord): (a) the maximum vertical deformation, (b) the stress of the concrete in the vault, and (c) the stress of the steel tube in the vault.

Figure 26 shows that the maximum deformation caused by temperature gradient is 53.3% larger than that under overall temperature rise; the maximum stress intensity of the steel tube caused by temperature gradient is 16 times larger than that under overall temperature rise; and the tensile stress of the concrete in the vault is large under temperature gradient, but it is mainly compressed under the overall temperature rise condition.

Results show that the temperature effect under temperature gradient is greater than that under overall temperature rise.

5.3.4. Transverse Perfusion Sequence. The steel tube arch ribs without concrete are activated to calculate the stress influence lines of arch foot during concreting arch ribs of 1#, 2#, 3#, and 4#. The peak values of the influence lines are shown in Table 4.

Results show that the peak values of the stress influence lines when pouring 1# and 3# arch ribs are basically the same, and they are smaller than when pouring arch ribs of 2# and 4#. Pouring 1# or 3# arch rib firstly is beneficial to the steel tube. According to the temperature field detailed in Chapter 3, the maximum temperature difference of 1# and 3# chord is 23.7°C and 11.8°C, respectively. So, 3# chord should be poured at first based on the above principles.

Table 4: The peak values of the stress influence lines and the maximum daily temperature difference of each chord.

Arch rib	1#	2#	3#	4#
Peak value (the first)	36	40	36.1	40.2
Peak value (the second)	33.2	36.4	Irrigated	36.7
The maximum temperature difference (°C)	23.7	21.2	11.8	17.2

The steel tube arch ribs and the concrete of 3# arch rib are activated to calculate the stress influence lines of arch foot during pouring arch rib of 1#, 2#, and 4#. The peak value of the stress influence line when pouring arch rib of 1# (33.2) is smaller than when pouring arch ribs 2# (36.7) and 4#

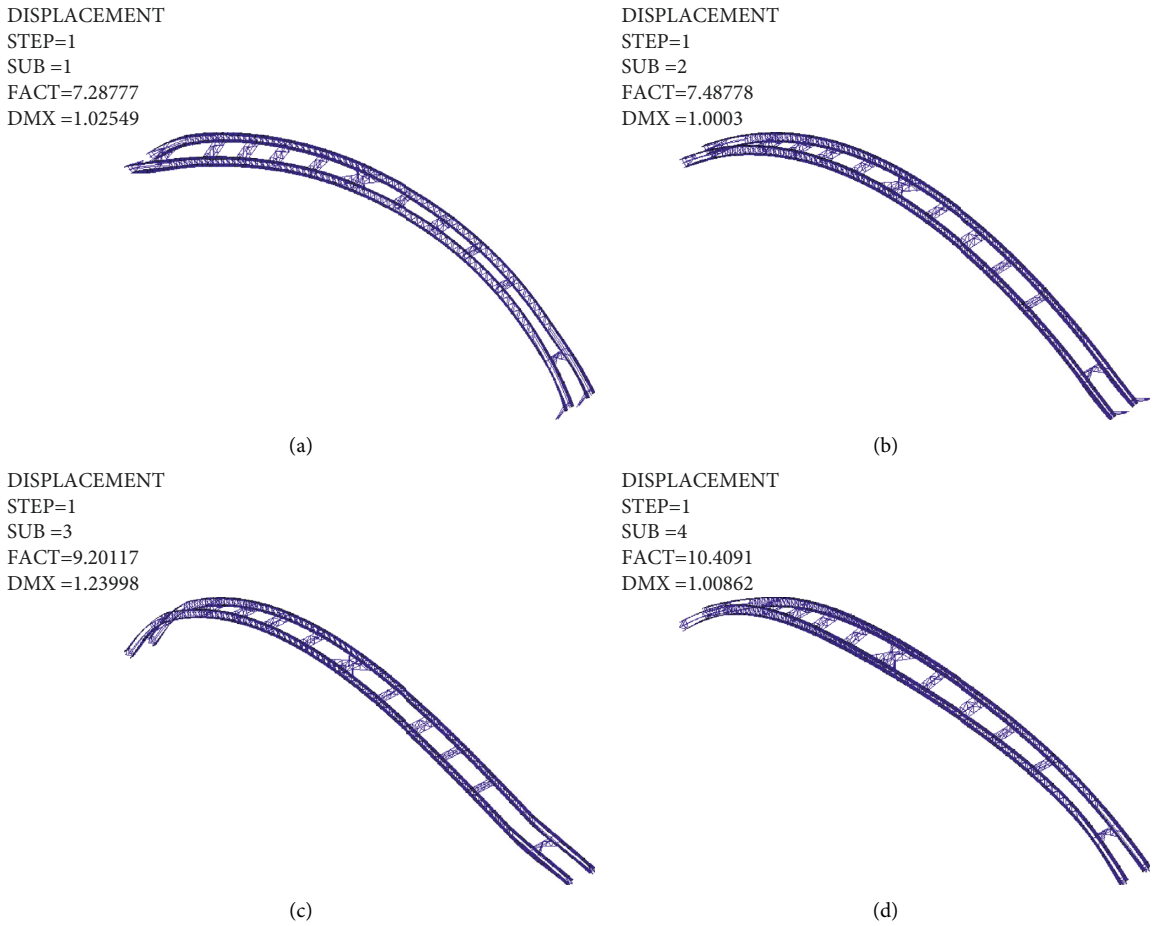

Figure 27: Stability calculation: (a) the first-order instability mode, (b) the second-order instability mode, (c) the third-order instability mode, and (d) the fourth-order instability mode.

(36.4). So, 1# chord should be poured second. The peak values of the stress influence lines when pouring 2# and 4# arch ribs are basically the same, but the maximum temperature difference of 2# chord (21.2°C) is larger than that of 4# chord (17.2°C), so 4# chord should be poured third, and 2# chord should be poured last.

The upstream and downstream components of this bridge were poured symmetrically at the same time to reduce erection time. Consequently, the transverse pouring sequence was 3 (8) # - 1 (6) # - 4 (7) # - 2 (5) # based on stress influence line and temperature field. With this perfusion sequence, the minimum stability coefficient during pouring is 7.3 (see Figure 27), which is greater than the stability requirement of 4.

Construction stability is improved, and pouring period is shortened by half with the research scheme proposed in this paper based on stress influence line and temperature field. In addition, 24 construction simulation analyses must be carried out using the traditional exhaustive method, which is heavy workload and is time-consuming. However, the determination of stress influence line and temperature field using the method proposed in this paper avoids tedious construction simulation analysis and, thus, is convenient for engineering applications.

5.3.5. Perfusion Interval. According to the design data, C50 was adopted for the core concrete of this bridge. Finite element analysis of primary arch forming is carried out, and the bending moment of each unit is obtained and substituted into (13), and U0 is calculated to be 22663.45.

It can be considered that the equivalent age is consistent with the real age as its construction condition is good and the concrete temperature during early hardening process reaches standard conditions.

Assuming that it takes 10 days to pour each arch rib, the time to pour the concrete of each rib is as $t_1 = D_1 + D_2 + D_3 + 30, t_2 = t_1 - 10 - D_1$ and $t_3 = t_1 - D_1 - D_2 - 20 t_4 = 0$.

Zero-order optimization is applied to determine the optimal perfusion interval based on the research method in Section 4.2. With state function of tensile stress meeting the required level, the objective is to minimize the difference of weighted bending moment strain energy between considering section installation and not considering section installation. The design variables iterate from 1 to 5 days with an initial value of 1 day. The optimal solution results of D1, D2, and D3 are 4 days, 3 days, and 3 days, respectively. It is usually 3 or 4 days in practical engineering. So, this weighted energy optimization method is a reasonable way to calculate pouring time of CFST arch bridges.

6. Conclusion

A systematic and comprehensive calculation program of temperature field and its temperature effect of CFST arch bridges under solar radiation, ambient temperature, and hydration heat were compiled in this paper, which can be used to calculate and load solar radiation intensity, judge shielding effect, and conduct transient thermal analysis. The optimization method of transverse pouring sequence and perfusion-time interval of CFST arch bridges considering temperature effect was proposed based on stress influence lines, temperature field, equivalent age theory, and energy method. The main conclusions are as follows:

(a) The radial temperature field of CFST arch bridges under solar radiation, ambient temperature, and hydration heat distributes as an asymmetric three-segment polyline with an influence depth of $D/8$, which is less than the specified value of $D/4$, and that under ambient temperature and hydration heat distributes as a symmetrical three-segment polyline with an influence depth of $D/4$. The temperature decreases from the interface on the sunny side to its $D/8$, then increases to the center, and then decreases from the center to the interface on the shaded side. The maximum temperature on the sunny side is about 20°C higher than that on the shaded side. The temperature of the concrete from the center to its $D/4$ along each radial direction is large and close at night, and the maximum temperature exceeds 50°C.

(b) The calculation method of transverse perfusion sequence based on stress influence line and temperature field proposed in this paper can improve the stability during pouring stage and is simple and efficient for an engineering application. The optimization method of perfusion-time interval considering influence of concrete temperature on moment energy based on the theory of concrete maturity and energy method proposed in this paper is conducive creating a reasonable construction time.

(c) The temperature stress of the concrete is unevenly distributed along radial direction, with the maximum tensile stress being 3.64 MPa. The stress of the steel tube on the sunny side is greater than that on the shaded side, with the maximum tensile stress being 146 MPa.

(d) The maximum temperature gradient of the concrete increases by 27.5% with the solar radiation absorption increasing from 0.55 to 0.75, and the daily ambient temperature difference increasing from 20°C to 40°C. Wind speed mainly affects heat exchange of outer steel tube and has little effect on the temperature of inner concrete.

(e) The maximum stress of the steel tube and concrete increases by 15% and 25%, respectively, with the solar radiation absorption coefficient increasing from 0.55 to 0.75. The maximum stress of the steel tube and concrete increases by 21.4% and 31.6%, respectively, with the daily temperature difference increasing from 20°C to 40°C. The maximum stress of the steel tube and concrete increases by 15.7% and 19.5%, respectively, with the -pwind speed decreasing from 7 m/s to 3 m/s.

(f) The results of the temperature field test agree well with the finite element, which proves that the transient thermal analysis algorithm established in this paper can be used to predict the temperature field in practical engineering situations. A temperature control system for CFST arch bridges that can prevent voids and cracks caused by a temperature gradient during concrete hardening can be established based on the distribution and evolution of the temperature field revealed in this paper, which needs further study.

Data Availability

The data used to support this study were available from the corresponding author upon request.

Conflicts of Interest

The authors declare that they have no conflicts of interest.

Acknowledgments

This research was funded by Chongqing Transportation Industry Science and Technology Project (KJXM2021-0966); the National Nature Science Foundation of Chongqing: Study on long-term temperature field and temperature effect of concrete filled steel tubular arch bridge in highly cold area (Project review No.: 2022NSCQ-MSX5138).

References

[1] B. C. Chen, J. G. Wei, and J. Zhou, "Application status and prospect of concrete-filled steel tube arch bridge in China," *Journal of Civil Engineering*, vol. 50, no. 6, pp. 50–61, 2017.

[2] K. Raoufi, J. Schlitter, and D. Bentz, "Parametric assessment of stress development and cracking in internally cured restrained mortars experiencing autogenous deformations and thermal loading," *Advances in Civil Engineering*, vol. 2011, 16 pages, 2011.

[3] T. Honorio, B. Bary, and F. Benboudjema, "Evaluation of the contribution of boundary and initial conditions in the chemo-thermal analysis of a massive concrete structure," *Engineering Structures*, vol. 80, pp. 173–188, 2014.

[4] N. Tayşi and S. R. Abid, "Temperature distributions and variations in concrete box-girder bridges: experimental and finite element parametric studies," *Advances in Structural Engineering*, vol. 18, no. 4, pp. 469–486, 2015.

[5] D. W. Zhou, N. C. Deng, and T. Shi, "A large-scale experimental study on temperature gradient of concrete-filled steel tube Arch bridge," *Journal of Railway Science and Engineering*, vol. 17, no. 8, pp. 2013–2019, 2020.

[6] D. W. Zhou, N. C. Deng, and X. Guo, "Temperature effect of large temperature difference on concrete-filled steel tubular arch bridge in Qinghai-tibet Plateau," *Journal of Guilin University of Technology*, vol. 40, no. 4, pp. 735–741, 2020.

[7] D. W. Zhou, N. C. Deng, and T. Shi, "Experimental study on hydration of CFST arch rib under low temperature in sichuan-tibet railway," *Railway Standard Design*, vol. 64, no. 12, pp. 56–62, 2020.

[8] T. Shi, J. L. Zheng, N. C. Deng, Z. Chen, X. Guo, and S. Wang, "Temperature load parameters and thermal effects of a long-span concrete-filled steel tube Arch bridge in tibet," *Advances in Materials Science and Engineering*, vol. 2020, p. 1, Article ID 9710613, 2020.

[9] J. Liu, Y. Liu, G. Zhang, L. Jiang, and X. Yan, "Prediction formula for temperature gradient of concrete-filled steel tubular member with an arbitrary inclination," *Journal of Bridge Engineering*, vol. 25, no. 10, Article ID 04020076, 2020.

[10] J. Liu, Y. Liu, and G. Zhang, "Experimental analysis of temperature gradient patterns of concrete-filled steel tubular members," *Journal of Bridge Engineering*, vol. 24, no. 11, Article ID 04019109, 2019.

[11] D. Yang, G. Chen, and X. Ding, "Thermal field of large-diameter concrete filled steel tubular members under solar radiation," *Computers and Concrete*, vol. 26, no. 4, pp. 343–350, 2020.

[12] B. Feng, *Research on Calculation Models for Hydration Heat, Shrinkage and Creep of Concrete-filled Steel Tubes*, Fu Zhou University, Fujian, China, 2004.

[13] K. Cheng and Y. D. Li, "Measurement and finite element calculation of sunshine temperature field of concrete filled steel tube arch rib," *Highway Traffic Science and Technology*, vol. 29, no. 9, pp. 77–84, 2012.

[14] B. C. Chen and Z. Y. Liu, "Study on temperature field of concrete filled steel tubular truss arch under sunshine," *Journal of China Highway*, vol. 24, no. 3, pp. 72–79, 2011.

[15] J. T. Zhou, J. Liu, and W. Zhou, "Analysis of temperature change on pre-lifting value of cable-stayed buckling and alignment of main arch ring of concrete filled steel tubular arch bridge," *Chinese and foreign highway*, vol. 37, no. 4, pp. 62–66, 2017.

[16] Q. Zhou, J. T. Zhou, and H. Ma, "An improved algorithm for the optimization of the primary tensioning force of the steel pipe arch rib section," *Journal of Transportation Engineering*, vol. 20, no. 1, pp. 93–99, 2020.

[17] H. B. Liu, Z. H. Chen, and T. Zhou, "Research on temperature field of steel tube under solar radiation," *Spatial Structure*, vol. 17, no. 2, pp. 66–71, 2011.

[18] J. T. Su, *Thermal Effect Analysis of CFST Arches in the Plateau with Large Temperature Difference*, Chang'an University, Xi'an, China, 2019.

[19] C. A. Gueymard, "Letter to the editor: on the clear-sky ASHRAE radiation model," *Energy Conversion and Management*, vol. 214, no. 2, Article ID 112822, 2020.

[20] J. S. Chen, J. T. Zhang, and J. K. Shao, "Research on temperature effect of bridge structure based on meteorological data," *Railway Construction Technology*, vol. 2021, no. 1, pp. 13–17, 2021.

[21] W. Akl, M. Ali, O. Aldraihem, and A. Baz, "Dynamic behavior of polyurea composites subjected to high strain rate loading," *Finite Elements in Analysis and Design*, vol. 186, no. 1, Article ID 103501, 2021.

[22] A. Gupta, P. D. Armatis, P. Sabharwall, B. M. Fronk, and V. Utgikar, "Energy and exergy analysis of Ca(OH)2/CaO dehydration-hydration chemical heat pump system: effect of reaction temperature," *Journal of Energy Storage*, vol. 39, Article ID 102633, 2021.

[23] Y. T. Zhang, L. Liu, and C. Y. Liu, "Estimation of hydration heat of cement," *Science and Technology Forum*, vol. 2012, no. 3, pp. 19-20, 2012.

[24] Q. Xu, S. Wang, H. Chen, and S. Wang, "Comprehensive analysis of electromagnetic and thermal-mechanical effects on HCSB under MD event for CFETR," *Fusion Engineering and Design*, vol. 138, no. 1, pp. 294–302, 2019.

[25] B. Jla and B. Jz, "A FE-IBE method for linearized nonlinear soil-tunnel interaction in water-saturated, poroelastic half-space: I. Methodology and numerical examples-ScienceDirect," *Soil Dynamics and Earthquake Engineering*, vol. 120, pp. 454–467, 2019.

[26] O. S. Lekhov and A. V. Mikhalev, "Calculation of temperature and thermoelastic stresses in the backups with collars of the unit of combined continuous casting and deformation in steel billet production. Report 2," *Steel in Translation*, vol. 51, no. 2, pp. 88–92, 2021.

[27] S. Mustafa, I. Yoshida, and H. Sekiya, "An investigation of bridge influence line identification using time-domain and frequency-domain methods," *Structures*, vol. 33, no. 3, pp. 2061–2065, 2021.

[28] J. Hong, R. Kim, C. H. Lee, and H. Choi, "Evaluation of stiffening behavior of concrete based on contactless ultrasonic system and maturity method," *Construction and Building Materials*, vol. 262, no. 6, Article ID 120717, 2020.

[29] V. Boswinkel, F. I. Sok, M. F. Krüse-Ruijter et al., "Ultrasound measurements of brain structures differ between moderate-late preterm and full-term infants at term equivalent age," *Early Human Development*, vol. 160, no. 1, Article ID 105424, 2021.

[30] M. Soutsos and F. Kanavaris, "Compressive strength estimates for adiabatically cured concretes with the Modified Nurse-Saul (MNS) maturity function," *Construction and Building Materials*, vol. 255, Article ID 119236, 2020.

[31] S. B. Zhao, Y. J. Gao, and J. H. Chen, "Experimental study and application of time-varying compressive strength and elastic modulus of C50 pumped concrete," *Concrete*, vol. 1, no. 1, pp. 98–101, 2015.

[32] Q. Zhou, J. T. Zhou, and J. C. Zhang, "Concrete self-adjusting load pouring method for long-span concrete-filled steel tubular arch bridge," *Journal of Harbin Institute of Technology*, vol. 52, no. 3, pp. 82–89, 2020.